
Abstract

Keywords:

1. Introduction

The search for alternate energy sources which could be categorised under the "green" label has become important area of research in the modern world. Solar, wind power and wave power are some of the examples of these sources. Recently, a new branch of research has been developing to extract energy from flow induced vibrations (Bernitsas et al. (2008)). It has been hypothesized that this technique may work efficiently in areas where regular turbines cannot.

A simple structure that is susceptible to flow-induced vibrations that are suitable for energy extraction are slender structures, such as cylinders, elastically mounted perpendicular to a fluid stream. With regards to a slender body two common types of flow induced vibrations are Vortex Induced Vibrations (VIV) and aeroelastic galloping. Significant research has been carried out by Bernitsas and his team on extracting useful energy from VIV. Some of their significant work includes investigating the influence of physical parameters such as mass ratio (the ratio of the mass of the cylinder and the displaced fluid), Reynolds number, mechanical properties (Raghavan and Bernitsas (2011), Lee and Bernitsas (2011)) and location (effect of the bottom boundary) (Raghavan et al. (2009)). However, the possibility of extracting energy using aeroelastic galloping has not been thoroughly investigated. Some theoretical work was carried out by (Barrero-Gil et al. (2010)). Utilizing galloping may be a more viable method to harness energy from flow induced vibrations as it is not bounded by a "lock-in" range of reduced velocities (ratio between the freestream velocity and the product of the natural frequency of the system and the characteristic length). Therefore it is preferable to investigate further the possibility of harnessing energy from flow induced vibrations using aeroelastic galloping.

Real life energy harvesting systems use high damping ratios where the energy generator (e.g electrical generator) puts a significant amount of damping into the system. Therefore it is crucial to investigate the behaviour of aeroelastic galloping scenarios at high damping ratios in order to optimise the system to obtain a acceptable power output. Hence the focus of this paper is concentrated on investigating the mechanical power output of high-damped galloping systems in laminar flow.

According to Païdoussis et al. (2010), Glauert (1919) has provided a criterion for galloping by considering the auto-rotation of an aerofoil. Den Hartog (1956) has provided a theoretical explanation for galloping for iced electric transmission lines. A non-linear

theoretical aeroelastic model to predict the response of galloping was developed by Parkinson and Smith (1964) based on the quasi-steady state (QSS) theory. Experimental lift and drag data on a fixed square prism at different angles of attack were used as an input for the theoretical model. It essentially used a curve fit of the transverse force to predict the galloping response. The study managed to achieve a good agreement with experimental (wind tunnel) data. Joly et al. (2012) have observed that finite element simulations shows a sudden change in amplitudes below a critical values of the mass ratio, which the (QSS) model fails to reproduce. The Parkinson's equation was essentially modified to account for the vortex shedding and managed to produce the effects to the amplitude at low mass ratios. Barrero-Gil et al. (2010) have investigated the possibility of extracting power from vibrations caused by galloping using quasi-steady state theory. In the conclusions of that paper it was pointed out that in order to obtain a high power to area ratio the mass-damping ($m^*\zeta$) parameter should be kept low as well as the frequency of oscillations should be carefully matched **have a good agreement with the size of the cross section**. Another interesting conclusion was that energy conversion systems which uses galloping could operate over a large range of flow velocities unlike VIV energy harvesting systems where the factor of energy conversion has a strong dependence on the incoming flow velocity.

Nomenclature

a_1, a_3, a_5, a_7	coefficients of the polynomial to determine C_y
C_y	instantaneous lift
F_y	force due to C_y
ρ	fluid density
m	mass of the body
m_a	added mass
c	damping constant/damping factor
k	spring constant
U_i	induced velocity
θ	induced angle of incidence
U	freestream velocity
y, \dot{y}, \ddot{y}	transverse displacement, velocity and acceleration
A	displacement amplitude
\mathcal{A}	cross sectional area
F_0	force due to shedding
ω_s	vortex shedding frequency
t	time
P_{mean}	mean power
$f = \frac{1}{2\pi} \sqrt{\frac{k}{m}}$	natural frequency of the system
$\omega_n = 2\pi f$	natural frequency of the system
D	characteristic length of the body
$m^* = \frac{m}{\rho \times \text{Volume of the body}}$	mass ratio
$U^* = \frac{U}{f \times D}$	reduced velocity
$\zeta = \frac{c}{2m\omega_n}$	damping ratio
P_t	power transferred to the body by the fluid
P_d	power dissipated due to mechanical damping
Re	Reynolds number
$\theta = \tan^{-1}(\frac{\dot{y}}{U})$	instantaneous angle

2. Background theory

2.1. Mathematical model (Quasi-steady)

One of the widely used mathematical model to predict the system response under galloping is the Quasi-steady state (QSS) model, incorporated by Parkinson and Smith (1964) for a square cross section. The equation of motion of the body under galloping is given by Eq. (1). The forcing term F_y is given by Eq.(2).

$$(m + m_a)\ddot{y} + c\dot{y} + ky = F_y \quad (1)$$

$$F_y = \frac{1}{2}\rho U^2 \mathcal{A} C_y \quad (2)$$



Figure 1: Induced angle of attack on the square prism due to the resultant of free-stream velocity of the fluid and transverse velocity of the body.

In the QSS model C_y is determined by an interpolating polynomial based on the stationary lift and drag data. The order of the interpolation polynomial has varied from study to study. For example a 7th polynomial order was used in Parkinson and Smith (1964) and 3rd order polynomial was used in Barrero-Gil et al. (2009). Ng et al. (2005) concluded that using a 7th order polynomial is sufficient and a polynomial higher than that of 7th order polynomial neither provides a significantly better result nor does it exhibit an additional amplitudes of oscillation. Thus a 7th order interpolating polynomial was incorporated in this present study.

***Tan: You need to talk about Figure 2. How your Re165 compares with earlier results. Highlight the main differences between Re165 and Re22300. What are the peak value in both. When do they become negative and why that is significant (i.e. idirection of power transfer). Also worh mentioning that the inflection point at ?? degrees leads to the hystersis and cite some key papers for that. Then say this is not present at Re165 and therefore expect no hyterisis at 165. The overall smaller C_y and smaller range of angles where C_y is +ve for Re165 compared to Re22300 leads one to expect a lot less power at re165 compared to re22300. Fix this up and then we can later in the results section relate back to here to aid in our explanation. ***

$$C_y(\theta) = a_1 \left(\frac{\dot{y}}{U} \right) + a_3 \left(\frac{\dot{y}}{U} \right)^3 + a_5 \left(\frac{\dot{y}}{U} \right)^5 + a_7 \left(\frac{\dot{y}}{U} \right)^7 \quad (3)$$

Joly et al. (2012) reported a reduction of displacement amplitude at low mass ratios. Therefore in order to account for it ***Tan: w ***hat is "it" ?? a sinusoidal forcing function to the RHS of the oscillator model (Eq. (1)) was introduced, in order to represent forcing due to VIV. This method provided satisfactory results with the numerical simulations obtained at low mass ratios. In this study, the forcing due to VIV is incorporated using a sinusoidal forcing function $F_0 \sin \omega_s t$ added to the RHS of the equation. ω_s and F_0 represents shedding frequency and the maximum force due to shedding respectively. Thus, the final equation is given by Eq. (4).

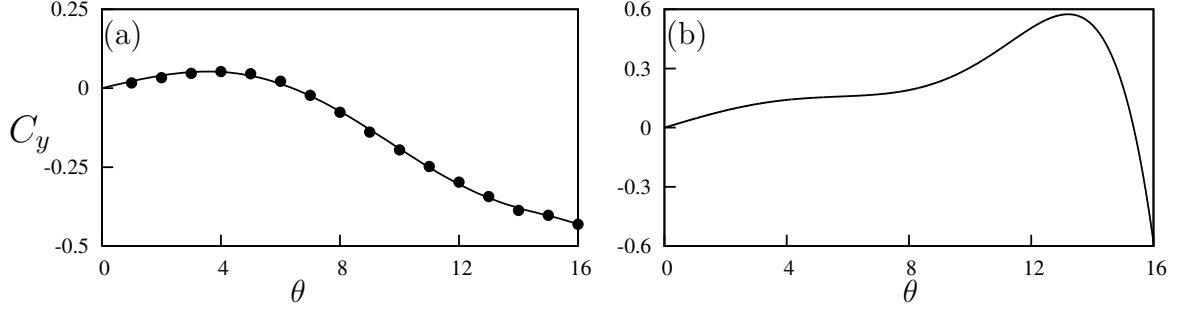


Figure 2: Lift coefficient, C_y ***JL: C_y is upper case here, lower case on the figure. Make them match what is in the nomenclature ***, as a function of incidence angle θ , for a static square cross section. (a) Data from simulations at $Re = 165$ (b) data from Parkinson and Smith (1964) at $Re = 22300$. Points (\bullet) are measurements from the simulations. The solid lines in both plots are 7th-order interpolating polynomial used to predict the fluid forcing for the QSS model.

$$(m+m_a)\ddot{y}+c\dot{y}+ky=\frac{1}{2}\rho U^2\mathcal{A}\left(a_1\left(\frac{\dot{y}}{U}\right)+a_3\left(\frac{\dot{y}}{U}\right)^3+a_5\left(\frac{\dot{y}}{U}\right)^5+a_7\left(\frac{\dot{y}}{U}\right)^7\right)+F_0\sin(\omega_s t) \quad (4)$$

This equation could be solved by time integration methods. In this study ‘Ode 45’ routine in MATLAB was used to obtain the solutions.

2.2. Calculation of average power

The dissipated power due to the mechanical damping could be expressed as the harvested power output assuming that the other power dissipation due to internal damping such as friction of the system is negligible. Therefore the mean power output could be given by Eq. (5).

$$P_{mean} = \frac{1}{T} \int_0^T (c\dot{y})\dot{y}dt \quad (5)$$

2.3. Parameters used

The stationary data and the fluid-structure interaction (FSI) data were obtained using a higher order spectral element code which simulate 2D laminar flow. The Reynolds number was kept at 165 as it was pointed out by Sheard et al. (2009) and Tong et al. (2008) that the 3 dimensional transition for a square cylinder occurs at approximately $Re=160$. F_0 was kept at 0.4937 which was obtained by using a simple linear interpolation on the data presented in Joly et al. (2012). ω_s was set to 0.98 which was obtained by performing a

Case	a_1	a_3	a_5	a_7
Re=165	1.3	125.3	1825.73	8765.3
Re=22300	2.69	168	1670	59900

Table 1: Coefficient values used in the 7th order interpolation polynomial for high ($Re = 22300$) and low ($Re = 165$) Reynolds numbers. These data are used as input data to calculate the RHS of Eq.4 throughout this study.

power spectral analysis of the stationary data at 0° . Stationary C_y data were obtained at different angles of attack ranging from 0° to 16° . The average power was obtained by using Eq. (5) with data sets consisting substantial amount of peaks. Power data at $Re=22300$ were obtained using input C_y data in Parkinson and Smith (1964) in order to provide a comparison between high and low Reynolds numbers. m^* was kept at 1163 for $Re=22300$ (Similar as Parkinson and Smith (1964)) and $m^* = 20$ for $Re=165$. These parameters were used throughout this study unless otherwise specified.

FSI data were obtained for the oscillating (free-vibration) scenario. The Naiver-Stokes equations were solved using an accelerated frame of reference using the previously mentioned code. A three-step time splitting scheme together with high-order Lagrangian polynomials were used to obtain the solution. The details of the method could be found in Thompson et al. (2006, 1996). This code was incorporated in Leontini et al. (2011, 2007) where it was employed in a fluid-structure interaction problems.

The computational domain consists of 690 quadrilateral macro elements where majority of the elements were concentrated near the square section. A freestream condition was given to the inlet, top and bottom boundaries and the normal velocity gradient was set to zero at the outlet. A convergence study was performed by changing the order of the polynomial (p -refinement) at $U^* = 40$ and Re 165. A 9th order polynomial together with a time step of $\frac{\Delta t U}{D} = 0.001$ was sufficient to ensure an accuracy of 2% with regards to amplitude of oscillation.

3. Results

3.1. Displacement, velocity and power output as a function of reduced velocity

The quasi-steady analysis data reveals that the displacement amplitude tend to grow with increasing U^* Fig.3 (a) and (b). The onset of galloping is delayed with increasing ζ for both high and low Reynolds numbers. This echo the findings of previous studies by Parkinson and Smith (1964) and Barrero-Gil et al. (2010). Hysteresis could be observed at higher Reynolds numbers.

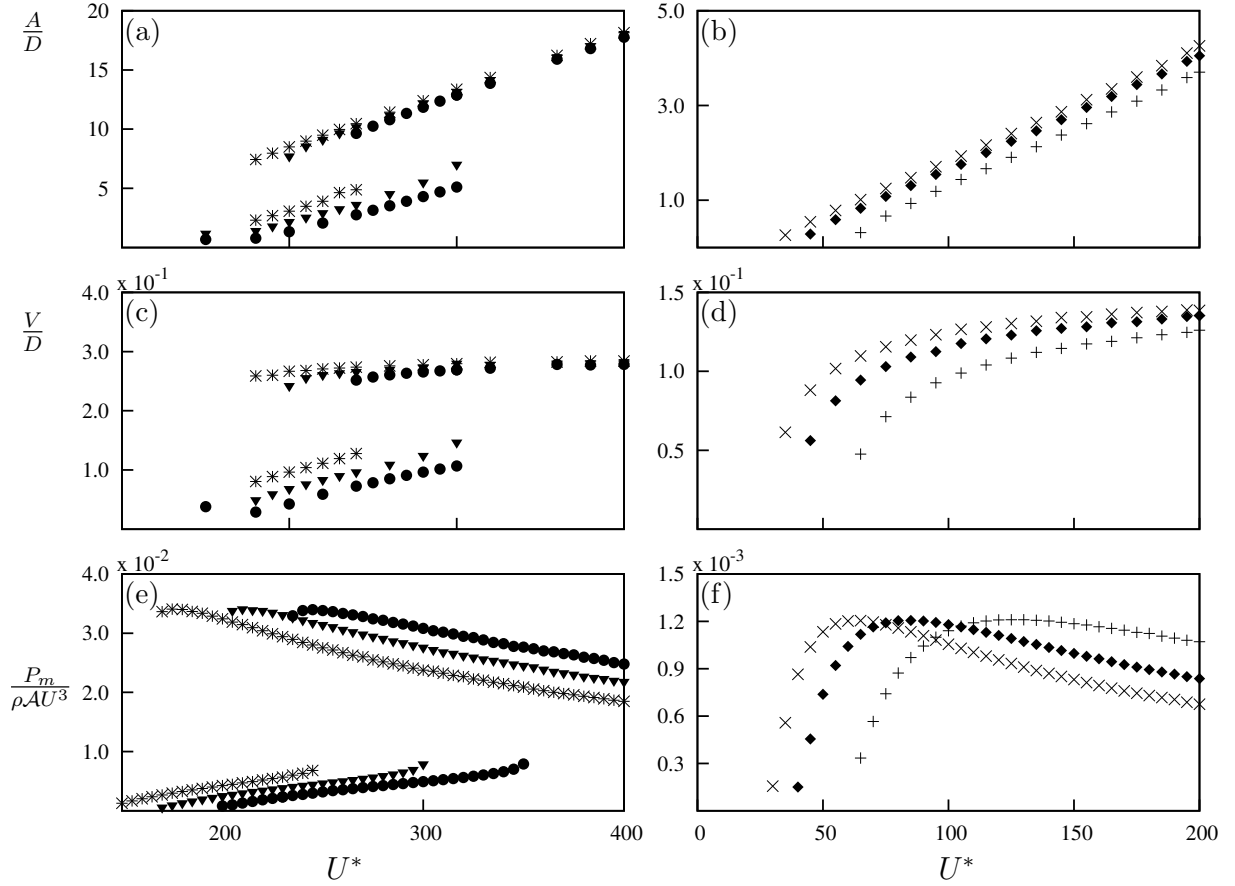


Figure 3: Velocity amplitude, displacement amplitude and mean power as functions of U^* . Data presented in (a), (c) and (e) were calculated using input data at $Re = 22300$ obtained by Parkinson and Smith (1964) at three different damping ratios: $\zeta = 0.0125$ (*), $\zeta = 0.015$ (\blacktriangledown) and $\zeta = 0.0175$ (\bullet). Data presented in (b),(d) and (f) were obtained using input data at $Re = 165$ at three different damping ratios: $\zeta = 0.075$ (\times), $\zeta = 0.1$ (\blacklozenge) and $\zeta = 0.15$ ($+$). The multiple branches for the higher Re are due to the hysteresis between two solutions.

*Power vs U^**

The mean power grows, peaks and then reduces as U^* is increased (Fig.3 (e) and (f)) for each value of ζ . A shift of the peak power could be observed as ζ increases. However, the magnitude of the peaks remain constant for all the values of ζ . A similar observation could be made from the results of Barrero-Gil et al. (2010). It could be observed that unlike VIV the system has no preferred frequency. Although the onset of galloping and the point where peak power occur at different U^* when the damping ratio is changed, the peak power remains constant regardless of U^* .

3.2. Galloping response and natural frequency

If the oscillator equation Eq.(4) is considered from a power perspective (disregarding the shedding term as the net effect is negligible as system oscillates at natural frequency which is far from shedding frequency), it is obvious the forcing term on RHS of the equation is only dependent on transverse velocity(\dot{y}) which is essentially the input power of the system. On the RHS, the mechanical damping or system damping is the only term that takes out power at any instant. This could be expressed as the product of damping force and the velocity (P_d). The inertia and the stiffness terms governs the frequency of the system but the forces associated by those terms are conservative forces i.e there is zero net energy in or out of the system when averaged over a period. Therefore that the system is governed by the transverse velocity rather than the natural frequency.

Using U^* and ζ assumes that the system has a preferred frequency. The effect of fixing ζ and increasing U^* actually decreases damping constant for a fixed free-stream velocity. ($U^* = \frac{U}{f \times D}$, $\zeta = \frac{c}{2m\omega_n}$). Both these effects leads to the multiple lines that are horizontally transpose when ζ is increased (Fig.3 (e) and (f)). Therefore the effect of ζ essentially scales up the damping coefficient for a fixed U^* .

A single set of results for a given C_y curve could be obtained for the displacement, velocity and power were plotted as a function of damping constant c (Fig 4 (a),(b),(c) and (d)). Fig.5 clearly shows that a similar velocity amplitude could be obtained for a given damping factor provided that the small fluctuations are disregarded.

Power could be expressed as the product of force and velocity. Therefore the transferred power from fluid-to-body could be expressed as $P_t = F_y \dot{y}$. Similarly the dissipated power due to the mechanical damping could be expressed as $P_d = (c\dot{y})\dot{y}$. The time average of these two quantities should be equal due to energy conservation, provided that the mechanical friction is neglected. Analysing the time histories of P_t and P_d at key regions (Fig.6) on the mean power vs U^* provides a detailed explanation for the variation of the output power when the reduced velocity is increased. The key regions consists of region 1 where the P_m increases with U^* , region 2 where P_m becomes maximum and region 3 where P_m decreases with U^* . It has been established earlier that the damping factor is a function of U^* . Therefore it could be derived that U^* is inversely proportional to damping coefficient. Hence the damping coefficient reduces when you move from region 1 to 3. Fig 2 (a) shows that C_y and therefore instantaneous force rises until 4° where it peaks and then falls and at around 6° becomes negative. Maximum amount of power could be transferred within

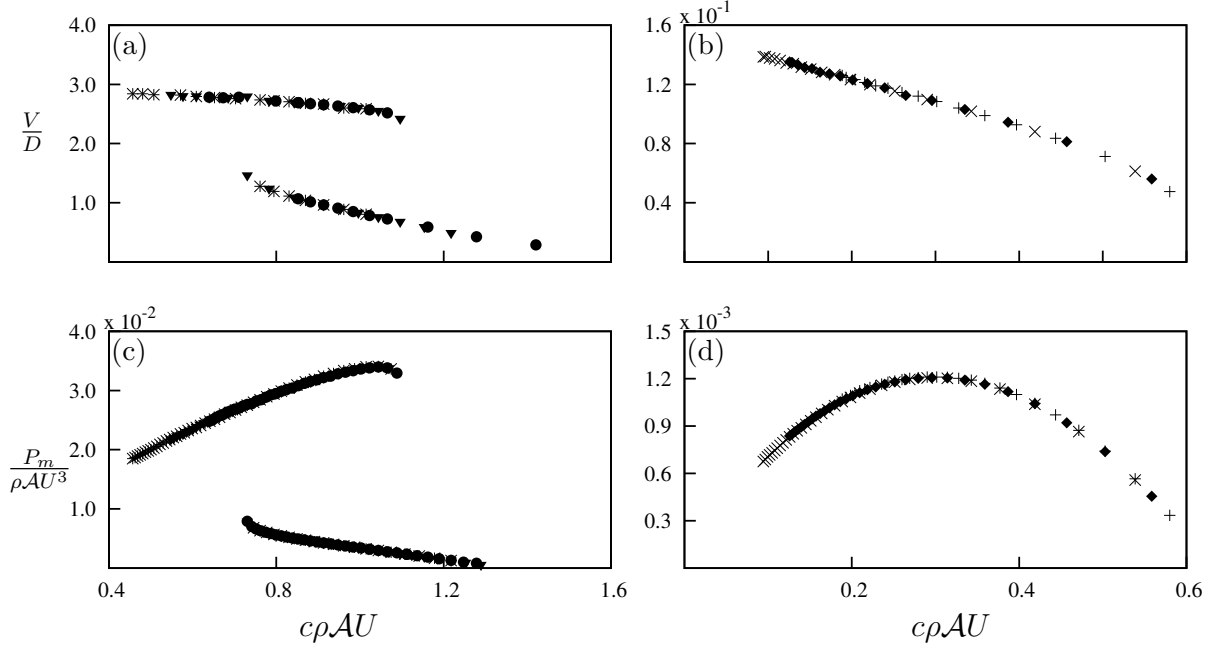


Figure 4: Velocity amplitude and mean power as functions of the damping factor. Data presented in (a) and (c) were calculated using input data at $Re = 22300$ obtained by Parkinson and Smith (1964) at three different damping ratios: $\zeta = 0.0125$ (*), $\zeta = 0.015$ (\blacktriangledown) and $\zeta = 0.0175$ (\bullet). Data presented in (b) and (d) were obtained using input data at $Re = 165$ at three different damping ratios: $\zeta = 0.075$ (\times), $\zeta = 0.1$ (\blacklozenge) and $\zeta = 0.15$ (+). The collapsed data implies that there is no frequency selection and the tuning parameter of the mechanical side of the system is the damping constant to obtain an optimum power output.

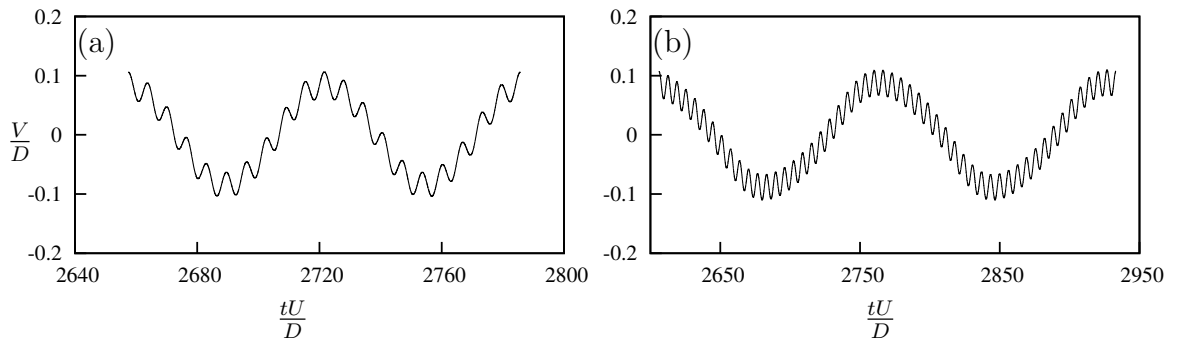


Figure 5: Time histories of velocity at two different ζ and U^* which produce the same mean power (1.2×10^{-3}). Data presented in (a) are at $U^* = 60$, $\zeta = 0.075$ and (b) are at $U^* = 165$, $\zeta = 0.175$. Both data sets were obtained using Quasi-steady state assumption using input C_y parameters at $Re = 165$. Shedding is evident in both signals as a high frequency fluctuation but the amplitude of the slower fluctuations remains constant in both cases.

the peak region. At the region where the instantaneous force becomes negative it will be opposing the velocity \dot{y} .

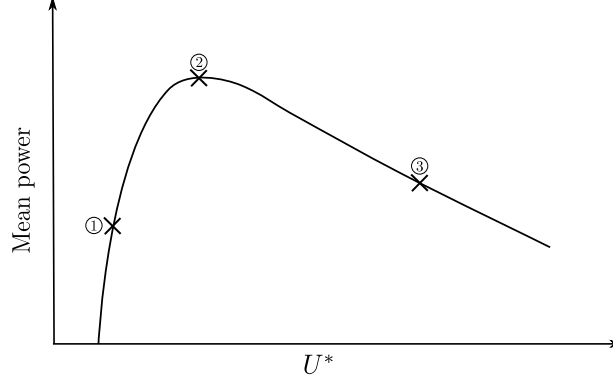


Figure 6: Three key regions taken into account to analyse the time histories of power in a typical mean power vs. U^* curve at $Re = 165$. In region 1, high damping suppresses oscillation, hence the power output is low. In region 2, the damping is close to the optimum for power transfer. In region 3, the low damping means little energy is extracted from the fluid.

At region 1 where $U^* = 90$ (region 1) the damping constant is high and therefore a clear sinusoidal signal could be observed for both P_d and P_t Fig. 7 (a). Fig.7 (d) and (g) shows that θ is in line or in phase with F_y . Hence both P_d and P_t becomes sinusoidal. However, due to the higher damping θ does not go to the region which produces the peak power.

At region 2 ($U^* = 165$) the mean power output is at its maximum. P_t is not a pure sinusoidal signal. However, the signal remains periodic. From the time history graph of P_t , two ‘peaks’ are present in a single half cycle (Fig 7 (b)). In this case at certain point in time θ arrives at the region where F_y decreases but does not become negative when the angle is increased. Therefore, the force F_y and P_t reduces as the velocity further increased. This is because $\theta = \tan^{-1}(\frac{\dot{y}}{U})$ and θ is proportional to transverse velocity. As the velocity \dot{y} is sinusoidal, θ recovers back and this leads to two ‘peaks’ in a single half cycle.

At region 3 ($U^* = 400$) ‘ c ’ is low in comparison with region 1 and 2 which leads to a low mean power output. Fig.7 (c) shows that P_t becomes negative over some portion of the cycle. This is because θ passes the point where both θ and C_y (therefore F_y) are positive. As the force opposes the direction of travel, the power becomes negative. On the other hand from an energy perspective we could see that the mechanical damping is not sufficient to dissipate out the energy transferred from the fluid to the structure (as ‘ c ’ is substantially low), therefore part of this energy is transferred back to the fluid which is depicted as a negative power region in Fig.7 (c).

3.3. Effect of m^*

The maximum mean power at different m^* (Fig.8) was constant beyond $m^* = 30$. However, at $m^* \leq 30$ an effect of m^* it could be observed. The peak value of the mean power curve reduces with m^* . This may be due to the fact that as the inertia of the system

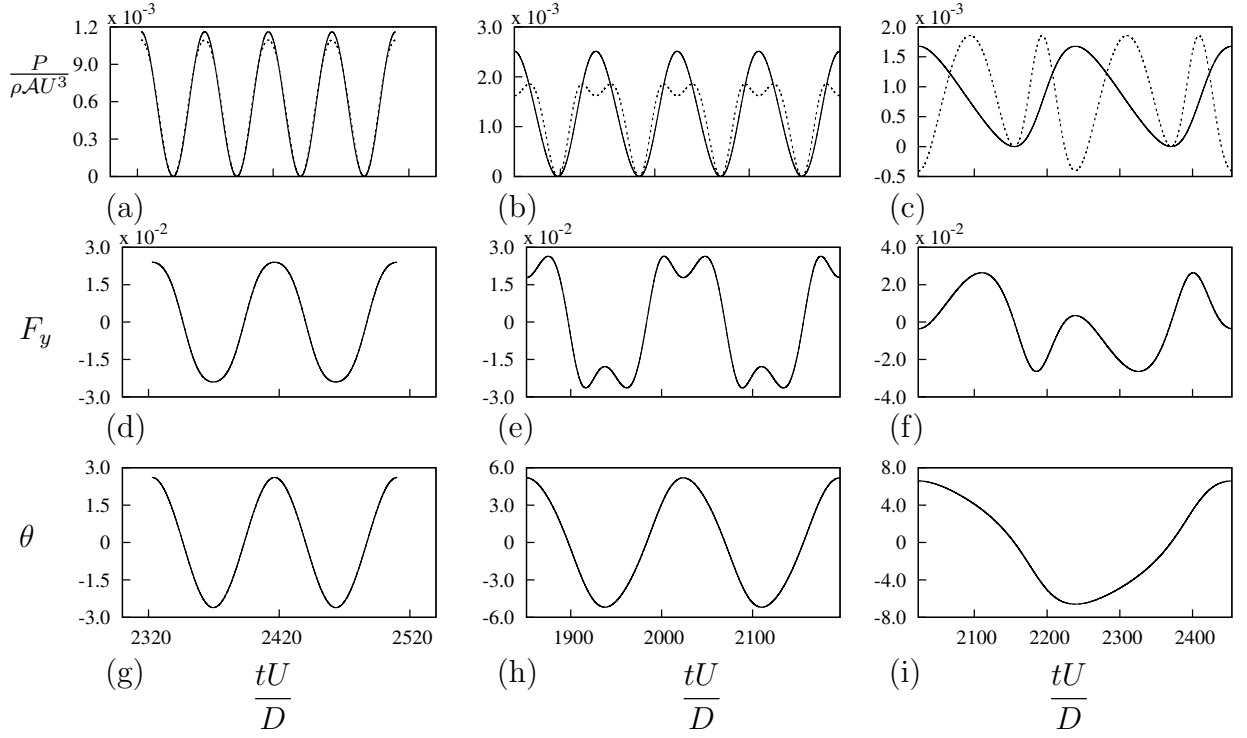


Figure 7: Time histories of P_t , P_d , F_y and θ at $U^* = 90, 165$ and 400 . Data was obtained at $\zeta = 0.1$, $m^* = 40$ and $Re=165$. The time histories of P_t (—) and P_d (---) are presented for: (a) $U^* = 90$; (b) $U^* = 165$; (c) $U^* = 400$. Time histories of the instantaneous force F_y for: (d) $U^* = 90$; (e) $U^* = 165$; (f) $U^* = 400$. Time histories of the instantaneous angle θ for: (g) $U^* = 90$; (h) $U^* = 165$; (i) $U^* = 400$.

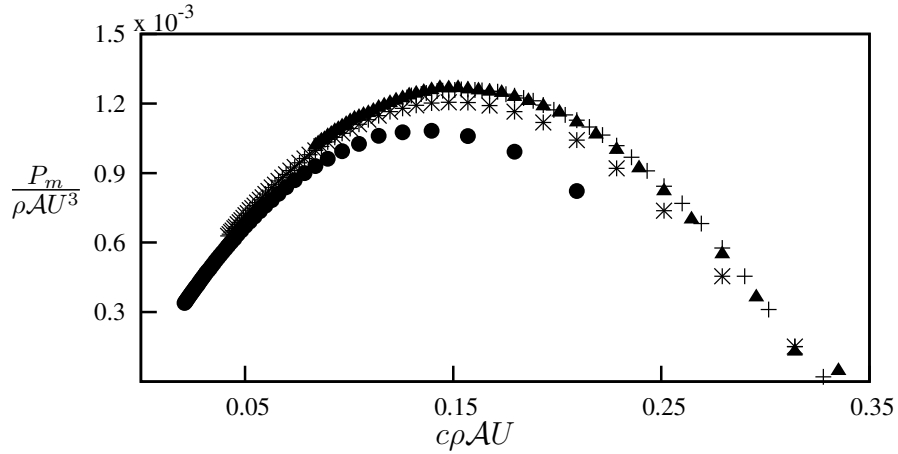


Figure 8: Mean power as a function of damping factor. Data are presented at $m^* = 10$ (●), $m^* = 20$ (*), $m^* = 40$ (▲), $m^* = 60$ (+) at $Re\ 165$ and $\zeta = 0.1$. A reduction of maximum mean power can be observed when $m^* < 40$. For $m^* > 40$, the maximum power is essentially independent of m^* .

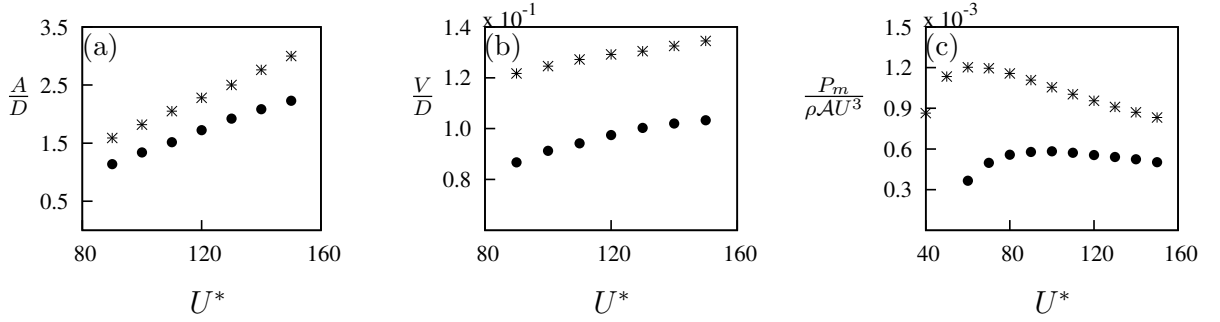


Figure 9: Comparison of data generated using the quasi-static theory (*) and full DNS simulations (●). (a) Displacement amplitude, (b) velocity amplitude and (c) mean power as functions of U^* . Data were obtained at $Re = 165$ and $\zeta = 0.075$. An average difference of 34% is observed for both displacement and velocity amplitude. However, the essential physics i.e the rise and fall of mean power, is captured by DNS simulations.

is reduced and galloping becomes weak. Therefore shedding become dominant. This was also reported by Joly et al. (2012) where galloping amplitude was reduced at low m^* .

3.4. Comparison with FSI simulations

Similar trends were captured for both displacement and velocity amplitudes between QSS and FSI simulations (Fig. 9(a) and 9(b)). Quantitatively a large discrepancy (average of 30%) could be observed between QSS and FSI data. Therefore the power also becomes significantly low in FSI data (Fig.9(c)). However, the FSI data (Fig.9 (c)) were able to produce the main the rise and the fall of mean power when U^* was increased. The reasoning behind this fact is that galloping is weak at Re 165 and therefore fluid damping has a significant effect. It was reported by Barrero-Gil et al. (2009) that galloping only starts to occur at $Re \geq 159$. As power is function of $(\dot{y})^2$ the error between QSS and FSI power becomes significantly large.

Put conclusion here

- Barrero-Gil, A., Alonso, G., Sanz-Andres, A., Jul. 2010. Energy harvesting from transverse galloping. *Journal of Sound and Vibration* 329 (14), 2873–2883.
- Barrero-Gil, a., Sanz-Andrés, A., Roura, M., Oct. 2009. Transverse galloping at low Reynolds numbers. *Journal of Fluids and Structures* 25 (7), 1236–1242.
- Bernitsas, M. M., Raghavan, K., Ben-Simon, Y., Garcia, E. M. H., 2008. VIVACE (Vortex Induced Vibration Aquatic Clean Energy): A new concept in generation of clean and renewable energy from fluid flow. *Journal of Offshore Mechanics and Arctic Engineering* 130 (4), 041101–15.
- Den Hartog, J. P., 1956. *Mechanical Vibrations*. Dover Books on Engineering. Dover Publications.
- Glauert, H., 1919. The rotation of an aerofoil about a fixed axis. Tech. rep., Advisory Committee on Aeronautics R and M 595. HMSO, London.
- Joly, A., Etienne, S., Pelletier, D., Jan. 2012. Galloping of square cylinders in cross-flow at low Reynolds numbers. *Journal of Fluids and Structures* 28, 232–243.
- Lee, J., Bernitsas, M., Nov. 2011. High-damping, high-Reynolds VIV tests for energy harnessing using the VIVACE converter. *Ocean Engineering* 38 (16), 1697–1712.
- Leontini, J. S., Lo Jacono, D., Thompson, M. C., Nov. 2011. A numerical study of an inline oscillating cylinder in a free stream. *Journal of Fluid Mechanics* 688, 551–568.
- Leontini, J. S., Th, M. C., Hourigan, K., Apr. 2007. Three-dimensional transition in the wake of a transversely oscillating cylinder. *Journal of Fluid Mechanics* 577, 79.
- Ng, Y., Luo, S., Chew, Y., Jan. 2005. On using high-order polynomial curve fits in the quasi-steady theory for square-cylinder galloping. *Journal of Fluids and Structures* 20 (1), 141–146.
URL <http://linkinghub.elsevier.com/retrieve/pii/S0889974604001215>
- Païdoussis, M., Price, S., de Langre, E., 2010. *Fluid-Structure Interactions : Cross-Flow-Induced Instabilities*. Cambridge University Press.
- Parkinson, G. V., Smith, J. D., 1964. The square prism as an aeroelastic non-linear oscillator. *The Quarterly Journal of Mechanics and Applied Mathematics* 17 (2), 225–239.
- Raghavan, K., Bernitsas, M., Apr. 2011. Experimental investigation of Reynolds number effect on vortex induced vibration of rigid circular cylinder on elastic supports. *Ocean Engineering* 38 (5-6), 719–731.
- Raghavan, K., Bernitsas, M. M., Maroulis, D. E., 2009. Effect of Bottom Boundary on VIV for Energy Harnessing at $8 \times 10^3 < Re < 1.5 \times 10^5$. *Journal of Offshore Mechanics and Arctic Engineering* 131 (3), 031102.

- Sheard, G. J., Fitzgerald, M. J., Ryan, K., Jun. 2009. Cylinders with square cross-section: wake instabilities with incidence angle variation. *Journal of Fluid Mechanics* 630, 43.
- Thompson, M., Hourigan, K., Sheridan, J., Feb. 1996. Three-dimensional instabilities in the wake of a circular cylinder. *Experimental Thermal and Fluid Science* 12 (2), 190–196.
URL <http://linkinghub.elsevier.com/retrieve/pii/0894177795000984>
- Thompson, M. C., Hourigan, K., Cheung, A., Leweke, T., Nov. 2006. Hydrodynamics of a particle impact on a wall. *Applied Mathematical Modelling* 30 (11), 1356–1369.
URL <http://linkinghub.elsevier.com/retrieve/pii/S0307904X06000321>
- Tong, X., Luo, S., Khoo, B., Oct. 2008. Transition phenomena in the wake of an inclined square cylinder. *Journal of Fluids and Structures* 24 (7), 994–1005.
URL <http://linkinghub.elsevier.com/retrieve/pii/S088997460800025X>